ACS Sustainable Chemistry & Engineering

pubs.acs.org/journal/ascecg

Research Article

Flexible Piezoelectric Nanogenerators Based on One-Dimensional Neutral Coordination Network Composites

Neetu Prajesh, Vijay Bhan Sharma, Shatruhan Singh Rajput, Chandan Kumar Singh, Prashant Dixit, Balu Praveenkumar,* Jan K. Zaręba,* Dinesh Kabra,* Satishchandra Ogale,* and Ramamoorthy Boomishankar*

Cite This: *ACS Sustainable Chem. Eng.* 2022, 10, 9911−9920

Read Online

ACCESS | Metrics & More | Article Recommendations | Supporting Information

ABSTRACT: Metal−organic coordination polymers are modular systems whose structures can be modified in numerous ways to introduce and influence non-linear optical and electrical properties. However, their full potential as piezoelectric nanogenerators for self-powered electronics is yet to be uncovered. Here, we report a Zn(II)-based ferroelectric one-dimensional coordination network $\{[Zn(\mathbf{L^1})(bpy)]\cdot(H_2O)_{1.5}\}_\infty$ (**1**) derived from a flexible dicarboxylate ligand $[PhPO(NH\text{-}(C_6H_4COOH))_2]$ ($\mathbf{L^1H_2}$) and 2,2′-bipyridine as a co-ligand. The origin of polarization in **1**, despite its neutral structure, is due to the polyhedral distortions around the Zn(II) center as revealed by ab initio calculations. The presence of polarizable domains was visualized by piezoresponse force microscopy (PFM) experiments. Also, from the PFM studies, a sizable converse piezoelectric coefficient (d_{33}) value of 19.4 pm/V was noticed for **1**, which is unprecedentedly high for the class of neutral-network coordination polymers. Furthermore, flexible composite devices comprising a thermoplastic polyurethane (TPU) polymer with different weight percentages (wt %) of **1** were prepared and examined for application as piezoelectric nanogenerators. Notably, the champion device of this series (poled 5 wt % **1**-TPU composite) exhibits a highest open-circuit voltage of 5.6 V and power density output of 14.6 $\mu W/cm^2$.

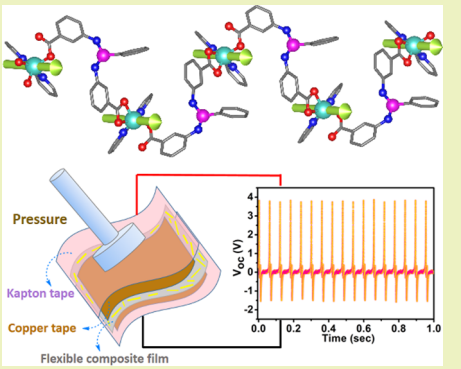

KEYWORDS: *coordination polymers, P-N ligands, piezoelectricity, ferroelectricity, energy harvesting*

INTRODUCTION

Piezoelectricity is a macroscopic property exhibited by intrinsically non-centrosymmetric crystals, in which the polarization is induced by the application of an external mechanical stress. Most commercial piezoelectrics are based on oxide ceramics and are utilized in microelectronics, telecommunication devices, medical ultrasonic imaging units, field-effect transistors (FETs), energy storage, photovoltaics, etc.[1−5] However, due to the presence of heavy and toxic metal in conventional ceramics, and their high processing temperatures, alternative materials that possess environmentally benign elements are investigated for piezoelectric applications.[6−8] In this regard, material selection spans from organic polymers, for example, commercially available semi-crystalline polyvinylidene fluoride (PVDF), to custom-made single-component organics, organic co-crystals, acid−base adducts, two-component salts (organic and hybrid organic−inorganic), and various supramolecular architectures, all of which have been investigated for their notable piezoelectric behavior.[9−14] Typically, these materials can be combined with piezoelectric or non-piezoelectric polymers to yield flexible composites and optimized multi-layered structures toward maximized energy scavenging performance.[15,16]

Metal−ligand coordination assemblies are among the emerging families of supramolecular systems that find a wide range of applications not only in chemical sensing,[17] gas adsorption and separation,[18] biomedicine,[19] and luminescence[20] but also in non-linear optics.[21−23] One of the key attributes of these materials is their efficacy to exhibit compositional tunability and structural diversity that can play a vital part in the design of framework solids with ferro- and piezoelectric properties. However, unlike traditional all-inorganic materials, it is challenging to impart ferroelectricity to the metal−ligand systems as structure−function relationships for them can only be drawn tentatively.[24,25] Despite the lack of highly dependable design rules, polar order in coordination networks can be achieved preferentially by systematic tuning of the nature of metal ions, coordinating ligands, counterions, and guest molecules.[7,26,27] However,

Received: April 18, 2022
Revised: July 8, 2022
Published: July 22, 2022

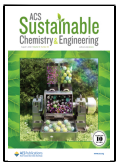

attaining ferroelectricity in neutral framework materials derived from carboxylate-based ligands has thus far been a challenging task; hence, such systems are far less explored than those with charged networks. The polarity in neutral MOFs can be induced by the incorporation of polar functional groups in carboxylate ligands or via encapsulation of polar solvent molecules like water and DMF (*N*,*N*-dimethylformamide), which interacts with the frameworks via non-covalent interactions.[25,28−30] Our group has been engaged in the design efforts of polar metal−ligand materials based on pyridyl donor ligands such as $[PhPO(NHPy)_2]$, (Py = 3-pyridyl (^{3}Py) or 4-pyridyl (^{4}Py)), $[PS(NH^3Py)_3]$, and $[PO(NHCH_2{}^3Py)_3]$, in which the piezo- and ferroelectricity originate from their stable charge-separated structure and the low symmetry of the employed phosphoramide scaffold.[31−36] Hence, we reasoned that developing pseudo-C_2 and C_3 symmetric phsosphoramide ligands containing carboxylic acid functional groups would result in the generation of neutral noncentrosymmetric coordination networks suitable for ferro- and piezoelectric studies. In this contribution, we describe a new neutral one-dimensional zinc coordination network $\{[Zn(\mathbf{L^1})(bpy)]\cdot(H_2O)_{1.5\infty}\}$ (**1**), employing the flexible carboxylate functionalized dipodal P-N ligand $[PhPO(NH\text{-}(C_6H_4COOH))_2]$ ($\mathbf{L^1H_2}$), which crystallizes in the polar non-centrosymmetric space group *R*3*c*. The piezoelectric behavior and the domain structure of **1** could be extracted at a microscopic level using the piezoresponse force microscopy (PFM) technique. Measurements of second-harmonic generation (SHG) at 800 nm not only provided independent, nonlinear optical evidence of structural non-centrosymmetry of **1** but also demonstrated two-photon excited luminescence (2PEL), pointing to its multifunctional behavior. Furthermore, flexible composites comprising the framework **1** in different weight percentages (wt %) were prepared with a thermoplastic polyurethane (TPU) polymer and examined for piezoelectric energy harvesting application. A highest open-circuit voltage (V_{oc}) of 5.6 V and power density output of 14.6 μW/cm^2 were achieved for the poled 5 wt % **1**-TPU nanogenerator device. Energy storage was demonstrated by charging the capacitors using the output voltages obtained from the 5 wt % **1**-TPU device. These findings are prominent contributions to the emerging area of metal−organic electricity nanogenerators.

EXPERIMENTAL SECTION

General Remarks. All reactions and work-up involving $PhPOCl_2$ were carried out under a dry N_2 atmosphere in Schlenk-type glassware. Ethyl 3-aminobenzoate, $Zn(NO_3)_2\cdot6H_2O$, and $PhPOCl_2$ were purchased from Merck chemical company and used as received. Dry solvents and $PhPOCl_2$ were distilled prior to use. All NMR spectra were recorded at room temperature using a Jeol 400 MHz spectrometer with operating frequencies of 400.13, 100.62, and 161.97 MHz for the respective ^{1}H, ^{13}C, and ^{31}P{^{1}H} nuclei. For the ^{1}H and ^{13}C spectra, $SiMe_4$ was employed as the internal standard, while for ^{31}P spectra, the 85% H_3PO_4 was used as the standard. The MALDI-TOF spectra of the ligands **L** and $\mathbf{L^1H_2}$ were recorded by using an Applied Biosystem MALDI-TOF/TOF spectrometer. The powder X-ray diffraction (PXRD) data of **1** were measured on a Bruker-D8 Advance diffractometer. A Perkin-Elmer STA-6000 thermogravimetric analyzer was used to obtain the TGA of **1**. Elemental analyses for **L**, $\mathbf{L^1H_2}$, and **1** were performed on a Vario-EL cube elemental analyzer. The melting points of **L**, $\mathbf{L^1H_2}$, and **1** were determined from an Electrothermal melting point apparatus. FT-IR spectra were recorded on a Bruker Alpha spectrophotometer in the attenuated total reflectance (ATR) mode for the neat samples of **L**, $\mathbf{L^1H_2}$, and **1**.

Synthesis. *L*. To a solution of ethyl 3-aminobenzoate (7.37 mL, 8.160 g, 24.53 mmol) in toluene (100 mL) kept stirring at 0 °C under an inert atmosphere, $PhPOCl_2$ (1 mL, 1.375 g, 3.52 mmol) in 10 mL of toluene was added dropwise using a pressure equalizer funnel. The resultant mixture was refluxed for 4 h until a white precipitate of the amine-hydrochloride was formed. The residue was filtered off, and the resulting filtrate was left standing at room temperature for 2−3 h to precipitate the ester compound **L**. It was then filtered off, washed three to four times with distilled water, and dried. Yield 1.71 g (54%). ^{1}H NMR (400 MHz, CD_3OD) δ 7.84 (dd, J = 13.6, 6.9 Hz, 2H), 7.74−7.73 (m, 2H), 7.53−7.47 (m, 1H), 7.46−7.40 (m, 4H), 7.30 (dd, J = 7.6, 2.3 Hz, 2H), 7.17 (t, J = 7.9 Hz, 2H), 4.19 (q, J = 7.1 Hz, 4H), 1.22 (t, J = 7.1 Hz, 6H). ^{13}C NMR (101 MHz, CD_3OD) δ 168.0, 142.9, 133.8, 133.0, 132.9, 132.5, 130.2, 129.8, 124.1, 123.5, 120.5, 62.1, 14.7. ^{31}P{^{1}H} NMR (162 MHz, CD_3OD) δ 12.01. MALDI-TOF: 475.31 $(M + Na)^+$, 491.31 $(M + K)^+$. M.P.: 190 °C. Anal. Calcd. for $C_{24}H_{25}N_2O_5P$: C, 63.71; H, 5.57; N, 6.19. Found: C, 63.84; H, 5.177; N, 6.04.

L^1H_2. The **L** (0.50 g) was dissolved in methanol (35 mL) and water (15 mL). Sodium hydroxide (400−500 mg) was added, and the resulting mixture was stirred overnight at room temperature. The $MeOH/H_2O$ was removed using a rotary evaporator, and the precipitate obtained was redissolved in 1 mL of H_2O and reprecipitated by adding an excess amount of 1 M solution of HCl. The product $\mathbf{L^1H_2}$ as a white solid was isolated by filtration and washed multiple times with water. Yield 0.295 g (59%).^{1}H NMR (400 MHz, DMSO-d_6) δ 12.78 (s, 2H), 8.28 (d, J = 11.5 Hz, 2H), 7.87 (dd, J = 7.3, 5.8 Hz, 1H), 7.83 (t, J = 1.7 Hz, 3H), 7.59 (td, J = 7.4, 1.4 Hz, 1H), 7.56−7.50 (m, 2H), 7.41 (dt, J = 6.9, 1.8 Hz, 4H), 7.27 (t, J = 7.9 Hz, 2H). ^{13}C NMR (101 MHz, DMSO-d_6) δ 167.3, 142.5, 133.0, 132.1, 131.7, 131.4, 129.0, 128.5, 122.1, 121.4, 118.6, 39.5. ^{31}P{^{1}H} NMR (162 MHz, DMSO-d_6) δ 8.77. MALDI-TOF: 420.01 $(M + Na)^+$, 434.11 $(M + K)^+$ M.P.: 220 °C. Anal. Calcd. for $C_{20}H_{17}N_2O_5P$: C, 60.61; H, 4.32; N, 7.07. Found: C, 60.19; H, 4.168; N, 6.98.

Compound 1. To a solution of $\mathbf{L^1H_2}$ (50 mg, 0.126 mmol) and 2,2′-bipyridine (19.5 mg, 0.126 mmol) stirred in *N*,*N*-dimethylformamide (DMF) (3 mL), $Zn(NO_3)_2\cdot6H_2O$ (111.55 mg, 0.378 mmol) in H_2O (3 mL) was added. This mixture was sealed in a 10 mL Teflon-lined stainless steel reactor and heated to 100 °C for 48 h in a programmable oven. The reaction system was cooled for 24 h. Fine needle-like white crystals suitable for SCXRD analysis were collected from the bottom of the reactor vessel. Yield: 70%. M.P. 229 °C. Calcd. for $C_{30}H_{26}N_4O_{6.5}PZn$: C, 56.05; H, 4.08; N, 8.71. Found: C, 55.96; H, 3.810; N, 8.04. FT-IR data on powder (cm^{-1}): 3228, 2361, 1580, 1382, 1207, 1126, 956, 814, 734, 685, 626.

Crystallography. The single-crystal X-ray diffraction data for **L**, $\mathbf{L^1H_2}$, and **1** were collected at 100 K on a Bruker Smart Apex Duo diffractometer using MoKα radiation (λ = 0.71073 Å). All the structures were refined using SHELX by full-matrix least-squares against F^2 on all data. All the non-hydrogen atoms of **L**, $\mathbf{L^1H_2}$, and **1** were refined anisotropically except for some of the atoms of $\mathbf{L^1H_2}$. Four carbon atoms in $\mathbf{L^1H_2}$ had poor thermal ellipsoids, and hence, they were refined with partial isotropic characteristics. The crystals of **L**, $\mathbf{L^1H_2}$, and **1** exhibited weak diffractions at higher angles. Hence, their data were reduced to 2θ = 50° for **L** and 2θ = 45° for $\mathbf{L^1H_2}$ and **1**.

Ferroelectric, Dielectric, and Piezoelectric Measurements. The ferroelectric P-E hysteresis loop measurements along with the leakage current plots for framework **1** were performed on its drop-casted film by using a commercial Sawyer−Tower circuit (TF Analyzer 2000E, aixACCT, Germany). The dielectric permittivity data for **1** was obtained on its polycrystalline pellets of 10 mm diameter using a Solartron analytical 1260 model impedance analyzer attached to a 1269A model dielectric interface. A Janis 129610A model cryostat integrated with a Lakeshore 336 model temperature controller was used as the sample holder. The d_{33} values of the poled composite films of **1**, of ∼0.47 mm thickness, were extracted on a PM300 Piezotest meter.

https://doi.org/10.1021/acssuschemeng.2c02296
ACS Sustainable Chem. Eng. 2022, 10, 9911−9920

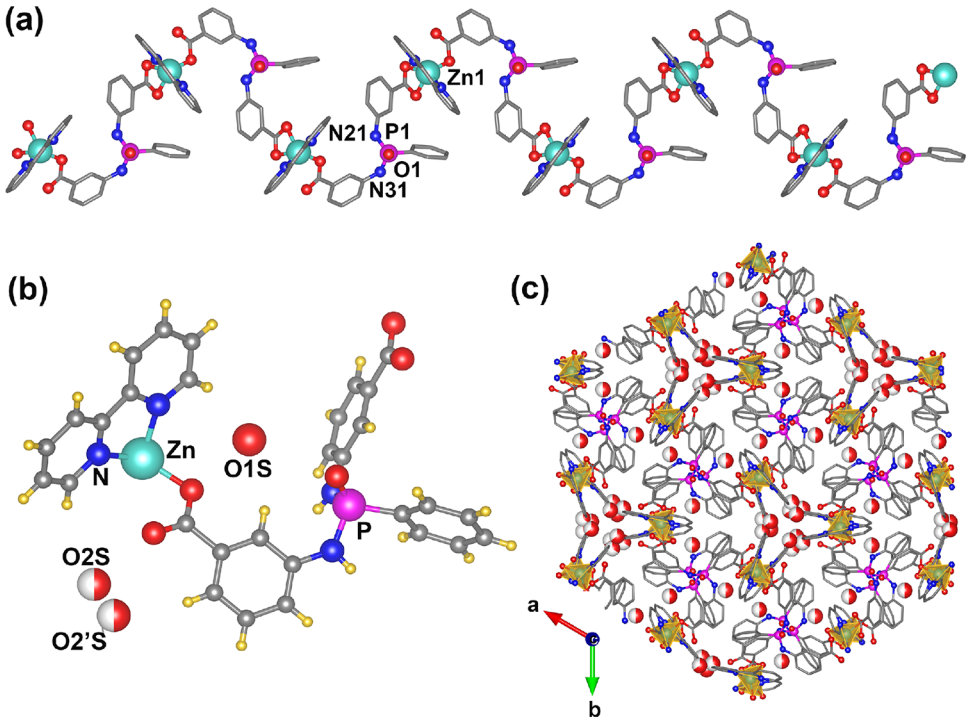

Figure 1. (a) Crystal structure of **1** showing its zig-zag one-dimensional coordination network. (b) Asymmetric unit of **1**. (c) Hexagonal packing structure of **1** viewed along the *c* axis. Color code: ligand backbone, gray; small blue spheres, nitrogen atoms; small red spheres, ligand oxygen atoms; zinc polyhedron, yellow; disordered water molecules, mixed white and red.

Second Harmonic Generation Study. The laser source used for SHG measurements was a Coherent Astrella Ti:sapphire regenerative amplifier generating 800 nm, 75 fs laser pulses (repetition rate of 1 kHz). Semi-quantitiative assessment of SHG efficiency was performed at 293 K following a modified Kurtz–Perry (Graja) powder test methodology. Potassium dihydrogen phosphate (KDP) was employed as an SHG standard. The single-crystalline materials of **1** and those of KDP were manually powdered and size-graded by sieving through an Aldrich mini-sieve set into 250–177 μm size range. Subsequently, sieved powders of **1** and KDP were placed in-between microscopic glass slides (forming tightly packed layers) sealed and placed on a horizontally aligned sample holder. A mean power density of an 800 nm laser beam was 0.49 W/cm^{-2}, with a spot area of 0.5 cm^2. The unfocused laser beam was directed at samples at 45°. Collimating optics, attached to the 400 μm optical fiber, were positioned at a right angle to the plane of the sample, allowing for detection of the backscattered SHG signal. A scattered 800 nm pumping beam was attenuated using a 750 nm short-pass hard-coated Thorlabs optical filter (FESH0750, O.D. >5 at 800 nm), which was placed in front of the signal collecting lens (f = 25.4 mm). An Ocean Optics Flame T-XR fiber-coupled spectrometer (200 μm entrance slit) was used to record the SHG signal.

Piezoresponse Force Microscopy Characterization. Piezoelectric characterizations of **1** and 5 wt % **1**-TPU film were studied under the Asylum research MFP-3D atomic force microscopy (AFM) system. The contact mode AFM (c-AFM) was done to obtain piezoresponse of the films. The measurement was done using RMN-12PT300B measurement cantilever probes with a 1.12 N/m spring constant and <8 nm tip diameter. The PFM data collected was based on the vertical PFM measurements (VPFM) where the ac voltage was applied to the conductive AFM tip, keeping the bottom electrode grounded. The PFM images were collected at a resonance frequency of 300 +/− 20 kHz with 2.5 V applied bias. The measurements were done in dual ac resonance tracking (DART) mode PFM.

Computational Details. The preliminary first-principles study for the electric polarization calculations was performed by employing the Berry phase method using the Quantum Espresso software code.[37] The nonrelativistic norm-conserving pseudopotentials with the Perdew–Burke–Ernzerhof (PBE) exchange-correlation functional were applied for the calculations.[38,39] The calculations were done using the modern theory of polarization on a discrete Zn(II) polyhedral core at the center of a box of dimension 18 × 18 × 18 Å^3 with a sufficient amount of vacuum in the free space to tackle the periodic effect. The change in dipoles was calculated upon changing the geometry around the Zn-core from an ideal square-pyramidal to a distorted square-pyramidal core as observed in the structure of **1**. Nevertheless, it should be emphasized that the overall dipole moment and the polarization of the system will include the collective contributions of the metal-ion, ligand systems, and the solvate atoms. Such calculations could not be performed due to the presence of atoms in huge number by the system. The structural graphics were acquired by using the VESTA software.[40]

Preparation of the 1-TPU Composite Films and Testing of the Composite Devices. Flexible polymeric composite films were prepared by the solution casting method. A constant quantity of TPU (1 g) was dissolved in *N*,*N*-dimethylformamide (6 mL, DMF) and heated at 90 °C for 60 min until a clear homogeneous solution was formed. A precalculated amount (for example, 53.47 mg for the 5 wt % composite) of ferroelectric crystals was added into a transparent homogeneous TPU mixture, and then, vortex mixing was performed for 5 min. The suspension was continuously stirred at room temperature for 4 h until the complete dispersion of the crystals. Afterward, the homogeneous composite mixture was poured into an aluminum mold and dried in an oven for 24 h at 60 °C. A completely dried free-standing milky white composite film from the aluminum mold was scraped off. A similar procedure was followed to prepare 1, 5, 10, and 15 wt % composite films. Further, the composite devices were fabricated with an appropriate selected area of 1.3 × 2 cm^2 and a thickness of ≈0.47 mm. The copper tapes with conductive adhesive were pasted on either side of the films using a hot-press method. The final device architecture for each wt % of the composite devices was encapsulated with a Kapton tape to protect the device from any physical damages. Further, by using a home-built impact measurement setup, the piezoelectric performance of all the composite devices of the framework **1** was carried out. The piezoelectric output voltages of the **1**-TPU films were recorded on a mixed-signal oscilloscope

https://doi.org/10.1021/acssuschemeng.2c02296
ACS Sustainable Chem. Eng. 2022, 10, 9911–9920

model Tektronix 2024 working at 1 MΩ input impedance. The currents generated during these measurements were monitored using a Keithley multimeter model number DMM7510 7.5.

RESULTS AND DISCUSSION

Synthesis, Characterization, and Crystal Structures. The flexible dipodal ligand $\mathbf{L^1H_2}$ was synthesized by reacting $PhPOCl_2$ with ethyl 3-aminobenzoate followed by hydrolysis (Scheme S1, Supporting information). The ligands were characterized by NMR spectroscopy, mass spectrometry, and single-crystal X-ray diffraction analysis (additional details on pages S4–S9 and Figures S1–S7, Supporting Information). Hydrothermal treatment of $\mathbf{L^1H_2}$ with $Zn(NO_3)_2{\cdot}6H_2O$ and 2,2′-bipyridine at 100 °C affords a one-dimensional zinc coordination network **1** (Scheme S2, Supporting Information). The single-crystal X-ray diffraction analysis of **1** reveals that it crystallizes in the trigonal *R*3*c* space group (a = 30.36 Å, c = 15.62 Å, and γ = 120°). The cationic charge of the Zn(II) center is canceled out by two carboxylate anions, while the 2,2′-bipyridine completes its coordination sphere. The Zn(II) ion is located in a penta-coordinated environment and exhibits a geometry in-between trigonal bipyramidal and square pyramidal but slightly inclined toward the latter, with the Addison parameter τ = 0.53 ($\tau = (\beta - \alpha)/60°$, where β and α are the two greatest valence angles around the coordinated metal center).[41]

The coordination sphere around the Zn(II) center consists of two nitrogen atoms from the 2,2′-bipyridine ligand and three carboxylate oxygen atoms from two $\mathbf{L^1}$ fragments. The two oxygen atoms from one arm of the dipodal ligand assume chelating coordination mode, and one oxygen atom from another $\mathbf{L^1}$ fragment lies in a terminal coordination (Figure S8, Supporting Information). Each unit of $\mathbf{L^1}$ interacts with two adjacent Zn(II) centers and gives rise to the framework of a 1D zig-zag chain structure (Figure 1a). Furthermore, the asymmetric unit of **1** contains 1.5 H_2O molecules, of which one of them is disordered over two positions (Figure 1b). These water molecules are involved in H-bonding interactions with both the coordinated and uncoordinated carboxylate O-atoms and result in the formation of a H-bonded trigonal 3D network along the *c* axis (Figure 1c). A closer look at the coordination polyhedron around the Zn(II) center shows that both the equatorial (chelating) Zn–O bonds are equivalent in distance (Zn–O21: 2.134(7) and Zn–O22: 2.172(8)), while the apical Zn–O contact (Zn–O31: 1.955(8)) is shorter by 9.2%. By contrast, one of the equatorial Zn–N distances of the 2,2′-bipyridine (Zn–N41: 2.084(6)) ligand is longer than the other one (Zn–N52: 2.007(7)) by 4.4%. The averages of out-of-plane bond angles, namely, O–Zn–O and N–Zn–O are 106.32(3)° and 113.975(3)°, respectively, are much larger than those found in typical square pyramidal geometries. In the absence of its typical charge-separated structure, these geometric distortions around the metal center could act as one of the factors causing polarization in **1**.

To check whether these distortions generate any dipole in the structure, we performed preliminary ab initio calculations on the polyhedral Zn(II) core of **1**.[42−45] These calculations yielded a change in dipole moment of 30.68 eÅ upon changing the Zn(II) core from an ideal square-pyramidal to distorted square-pyramidal geometry, as shown in Figure 2a. The location of the positive and negative charge densities obtained due to the distortions is displayed in Figure 2b. Interestingly, these dipoles align in the propagation direction of the 1D chain

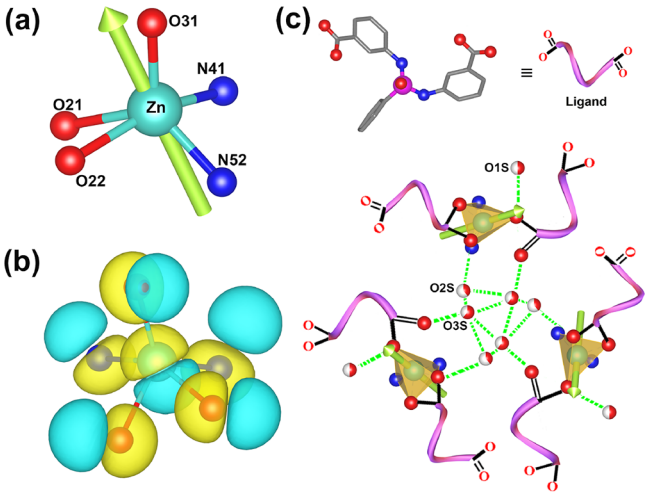

Figure 2. View of the Zn(II) core of **1** showing (a) the orientation of its dipole and (b) the charge-density plot with the separation of positive (yellow) and negative (cyan) charges. (c) Long-range ordering of the dipoles around the metal centers assisted by H-bonding interactions.

in **1** along the polar *c* axis (Figure S9, Supporting Information). Furthermore, a long-range order of these dipoles is established via H-bonding interactions with solvent molecules (Figure 2c). Nevertheless, it should be emphasized that the overall dipole moment and the polarization of the system will include the collective contributions of the metal-ions, ligand systems, and the solvate molecules.

SHG, Ferroelectric, Dielectric, and Piezoelectric Studies. The noncentrosymmetric nature of **1** was further verified by the Kurtz–Perry (Graja) powder method.[46,47] The 800 nm fs laser pulses were employed to obtain second harmonic generation (SHG) signals in size-graded samples of **1** and KDP (λ_{SHG} = 400 nm) at 293 K. The calculated integral intensities of SHG signals yielded a relative SHG efficiency of **1** equal to 0.23 versus that of the KDP reference material (Figure S10, Supporting Information).

The compound **1** exhibits a molecular symmetry of C_{3v}, which belongs to the combined class of 10 polar point groups that are capable of showing a ferroelectric property. To establish the ferroelectric nature of **1**, the polarization vs electric field (P-E) measurements were performed for **1** on its drop-casted thin films on the Al substrate (Figures S15 and S16, Supporting Information).[48] These measurements yielded a nearly rectangular shaped P-E hysteresis loop for the thin-film sample of **1**, indicating its ferroelectric nature. A saturation polarization (P_s) value of 4.80 $\mu C/cm^2$ at a coercive field of 0.62 kV/cm was obtained for **1** (Figure 3a). The current

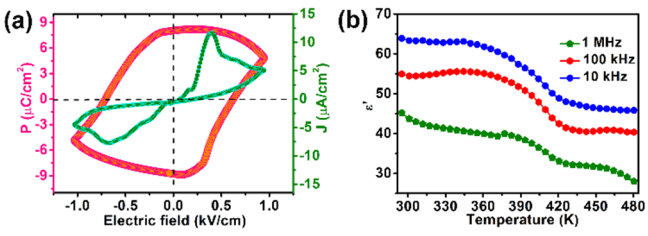

Figure 3. (a) P-E hysteresis loop measurements of **1** at room temperature along with the leakage current-density plot. (b) Temperature dependence of ε' for **1** under different frequencies.

https://doi.org/10.1021/acssuschemeng.2c02296
ACS Sustainable Chem. Eng. 2022, 10, 9911−9920

density measured as a function of the electric field along the P-E loop trace shows low leakage currents and gave peaks due to the coercive fields indicating the presence of switchable polarization.

To further explore the polarization characteristics, the dielectric permittivity analysis was done on the compacted disc of **1**. The real part of the dielectric permittivity (ε') as a function of temperature showed a broad anomalous peak at the temperature ranging from 308 to 423 K, which is attributed to the desolvation of the solvated water molecules present in **1**. Further rise in the temperature shows no additional peak anomaly, signifying the absence of any ferroelectric to paraelectric phase transition until 573 K (Figure 3b). The thermogravimetric analysis shows an initial weight loss of about 5% onset at 318 K and a subsequent weight loss of around 38% at 578 K due to its decomposition (Figure S17, Supporting Information). The powder X-ray diffraction data of framework **1** collected at temperatures between 300 and 493 K shows no change in its peak profiles, indicating that the crystallinity and the structural stability of the framework are retained even after desolvation (Figure S18, Supporting Information). Furthermore, the frequency-dependent permittivity measurements recorded in the range of 1 MHz to 10 kHz show an increasing trend in the ε' values, signifying the existence of all four polarization mechanisms in **1** at lower frequencies. Particularly, the polarizability of solvated water molecules and the mobility of ions gave higher polarization at lower frequencies (Figure S19, Supporting Information). The dielectric loss factor (tan δ), which indicates the dissipation of electrical energy as heat, was observed to be very low in both temperature- and frequency-dependent measurements (Figures S20 and S21, Supporting Information).

With the aim to investigate the local polarization state of **1**, vertical piezoresponse force microscopy (VPFM) experiments were done on the polycrystalline disc of **1** mounted on the Pt substrate. PFM provides the information regarding strength of the electromechanical coupling and direction of polarization in each domain.[49,50] An external dc bias of 50 V with a superimposed constant alternating current voltage of 2.5 V from the metal-coated conducting tip perpendicular to the pellet surface was applied to record the polarization attributes (Figure S22a, Supporting Information). The obtained amplitude and phase images of **1** with an active area of 5 × 5 μm^2 are shown in Figure 4a and Figure 4c, respectively (for topography, please see Figure S22b, Supporting Information). Subsequently, PFM spectroscopy was performed at a fixed location on **1** by applying an additional dc bias of 50 V at the cantilever tip. Figure 4b shows the typical "butterfly"-shaped amplitude-bias loop, which corresponds to the strain-voltage phenomenon of piezoelectric materials. The difference between phases of the opposite signals is nearly 180°, which shows the inverse domain switching of the polarization (Figure 4d). These results support the existence of ferroelectric behavior in **1**. Such observations for the domain structures at the nanoscale are rare among metal−ligand coordination polymers.[29] Furthermore, the piezoelectric coefficient d_{33} (a quantitative measure of the piezoelectric deformation, which is directly proportional to the amplitude) was calculated to be 19.4 pm/V. The observations of ferroelectric domains and sizable piezoelectric coefficient values are quite rare among single-component metal−ligand assemblies (Table S2, Supporting Information).

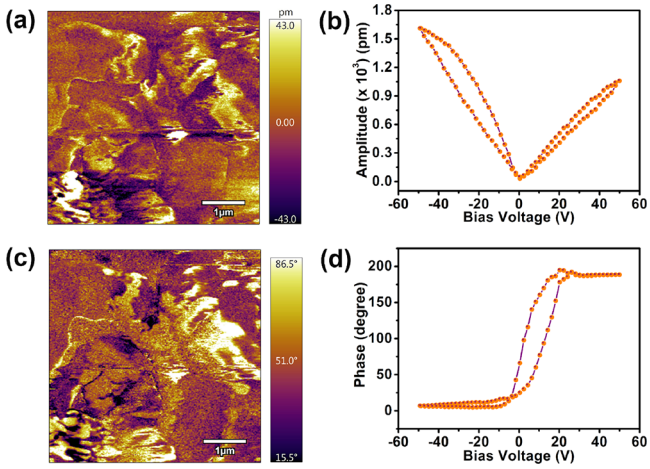

Figure 4. PFM data of **1**. (a) Amplitude image. (b) Amplitude-bias butterfly loop. (c) Phase contrast image (d) Phase hysteresis loop.

Fabrication and Characterization of the 1-TPU Composites. Spurred by the promising ferro- and piezoelectric attributes of **1**, we set out to utilize this framework for the fabrication of flexible piezoelectric nanogenerators. For this purpose, composites with various (1, 5, 10, and 15) weight percentages (wt %) of **1** were prepared in combination with the piezoelectrically inactive polymeric TPU.[51] These composites were obtained by mixing the calculated amount of **1** into a DMF solution of TPU. The homogeneous mixtures were poured into an aluminum mold and heated at 60 °C for 24 h, and the formed films were subsequently peeled off (Table S3 and Figure S23, Supporting Information). The exceptional flexibility of all these as-made composite films was examined by subjecting them to the various mechanical stretching, rolling, and bending operations (Figure 5a and Figure S24, Supporting Information). Furthermore, a good dispersion of **1** in the TPU matrix is observed from the confocal microscopy image of the 5 wt % **1**-TPU composite, which is favorable for the effective stress transfer during the mechanical energy generation process.[52,53] The PXRD profiles of these films show that all hkl diffraction peaks of **1** are intact in the composite films, serving as direct evidence for the presence of crystalline particles embedded in the composite films (Figure 5b and Figure S25, Supporting Information).

To confirm whether the piezoelectric properties of **1** are preserved in the composite films, the PFM experiments were performed on the 5 wt % **1**-TPU film. The amplitude image shows the presence of the domain structures with upward and downward polarizations. The PFM spectroscopy performed at a single point on the film shows the characteristic butterfly-shaped amplitude loop (Figure 5c,d and Figure S26, Supporting Information). The slope of the amplitude curve yielded a converse piezoelectric coefficient (d_{33}) value of 16.7 pm/V.

The device architectures for these composite films were made by placing copper adhesive tapes, which serve as top and bottom electrodes (Figure 5a). Finally, the fabricated nanogenerator devices were sealed with Kapton tape to keep the electrodes and the composite films intact and provide insulation to the devices from the external environment. The cross-sectional SEM images of a representative **1**-TPU device indicate the thickness of the **1**-TPU thin film to be ≈0.47 mm (Figure S27, Supporting Information). The output perform-

https://doi.org/10.1021/acssuschemeng.2c02296
ACS Sustainable Chem. Eng. 2022, 10, 9911−9920

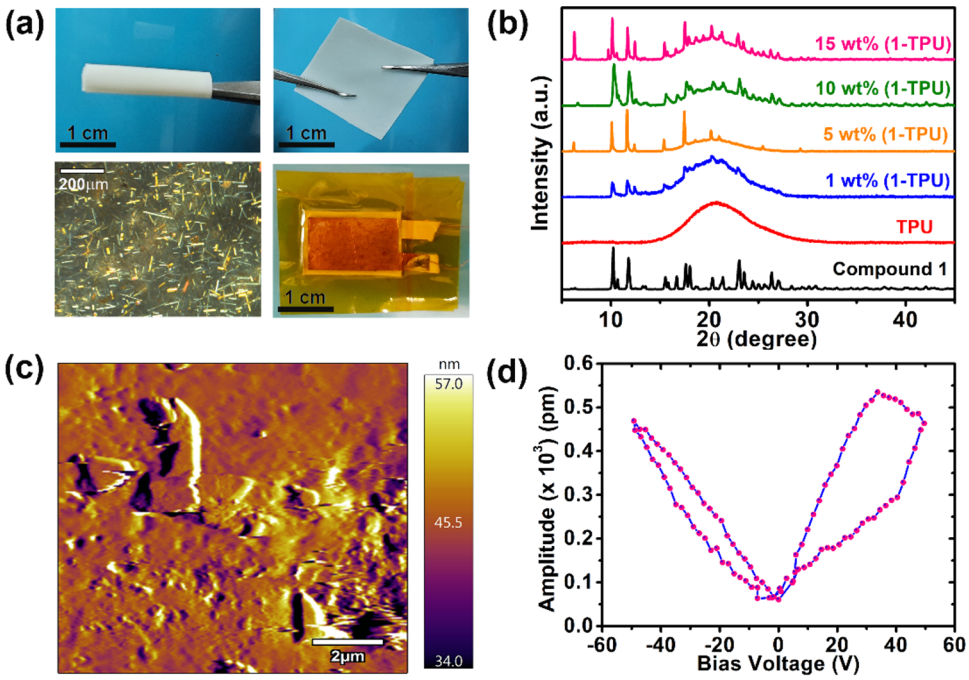

Figure 5. (a) From top to bottom: Pictures demonstrating the flexibility of a representative **1**-TPU film toward rolling and stretching functions. The **1**-TPU film photograph taken under the polarizing microscope at a magnification scale of 200 μm. Photograph of the device showing the sandwich structure of **1**-TPU between Cu electrodes encapsulated with Kapton tape. (b) PXRD profiles of composite films of **1**-TPU with various wt % of **1**. (c) PFM-topography image at a 10 × 10 μm^2 area of the 5 wt % **1**-TPU composite film. (d) PFM-amplitude-bias voltage butterfly-shaped loop.

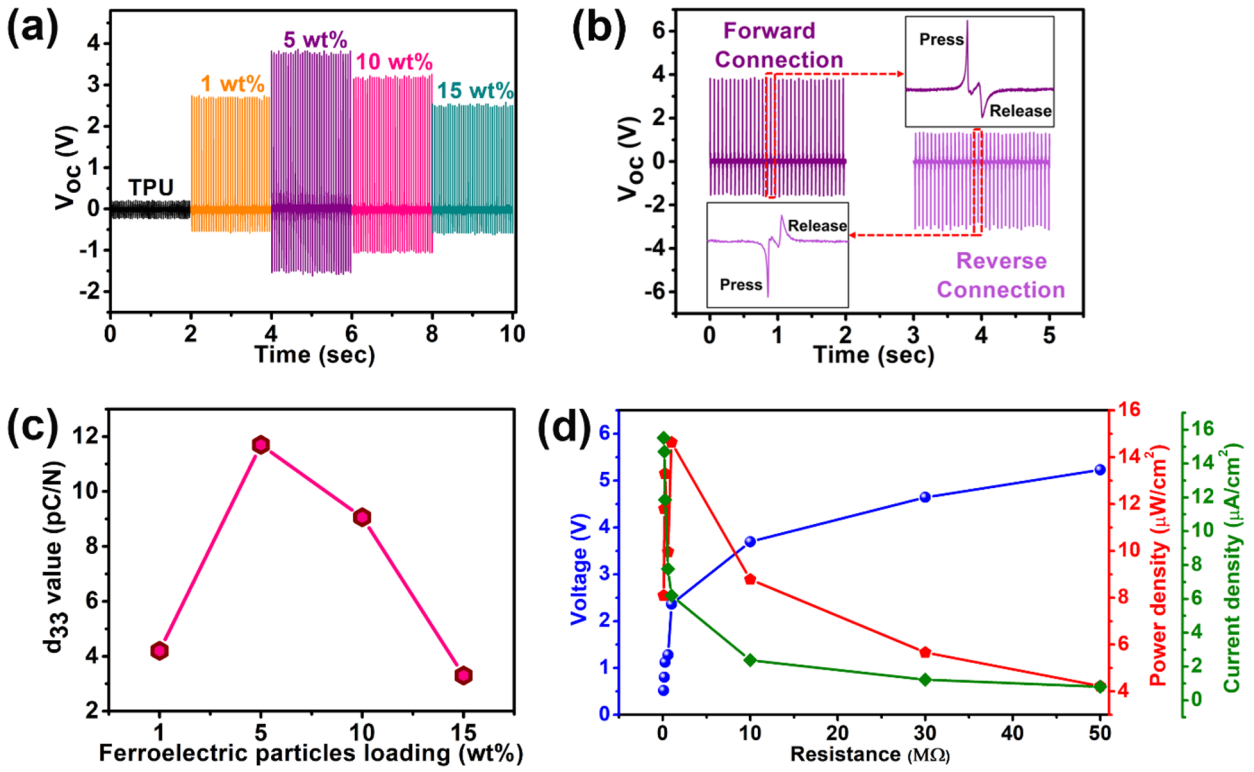

Figure 6. Piezoelectric characterizations of the poled **1**-TPU-based composite devices. (a) Open-circuit voltages (V_{oc}) of all the devices generated under a periodic mechanical tapping on a shifted-time axis. (b) Polarity-switching tests using the forward and reverse connections to the oscilloscope. (c) Longitudinal piezoelectric coefficient (d_{33}) measurements of various **1**-TPU films. (d) Load resistance-dependent output voltage, current density, and power density data of the best performing 5 wt % **1**-TPU film. The solid lines connecting the points in the plots of panels (c, d) serve as a guide to the eye.

https://doi.org/10.1021/acssuschemeng.2c02296
ACS Sustainable Chem. Eng. 2022, 10, 9911−9920

ance of all these **1**-TPU devices was estimated by applying constant compressive force from a home-built impact stimulator.[54] Prior to the experiment, all the **1**-TPU composite films were subjected to a poling process at an electric field of 25 kV/cm for about 2 h at room temperature to orient the disordered electric dipoles along the electric field direction. The open-circuit voltage (V_{oc}) of the devices was recorded under an impact force of 40 N at a frequency of 17 Hz, from each of the devices with an active area of 1.3 × 2 cm^2. Figure 6a presents the output voltages generated from all the **1**-TPU devices along with a blank device fabricated from a pristine TPU layer (for individual data, please see Figure S28, Supporting Information). It is evident that the electric performance is strongly correlated with the concentration of the piezoelectric fillers. An initial increase in the V_{oc} from 3.24 to 5.65 V is noticed as the mass fraction is varied from 1 to 5 wt % of **1**. Subsequently, it drops to 4.22 and 3.05 V as the content of **1** is increased further to 10 and 15 wt %, respectively. This clearly signifies that compositional optimization is essential for yielding the best performance in piezoelectric nanogenerators. In this case, the champion device is the 5 wt % **1**-TPU hybrid material, which shows a maximum output of 5.65 V. Also, an examination of the output voltages of this best-performing device under various external impact forces (28, 35, and 40 N) showed again the highest open-circuit voltage of 5.6 V at the optimal 40 N force (Figure S29, Supporting Information).

By contrast, the reference device involving only pure TPU shows a negligible V_{oc} of ∼400 mV. Since TPU is non-piezoelectric, the observed small electrical signals from it can be tracked to the residual electrostatic charges at the electrodes. Nevertheless, this effect can be neglected, given the large contrast provided by the robust piezoelectric effect seen for **1**. Furthermore, we carried out a polarity-switching test (by reversing the connections to the oscilloscope) on all the **1**-TPU devices to verify that the observed electric signals are purely due to the piezoelectric effect (Figure S30, Supporting Information).[55,56] Figure 6b illustrates that the V_{oc} values of nearly the same magnitude are observed from the best performing 5 wt % **1**-TPU nanogenerator in the forward and reverse connections. The insets of this figure exhibit a close view of a single pulse demonstrating the reversibility of the positive and negative piezoelectric potential responses during the compression and release cycles. Also, the obtained V_{oc} from the non-poled devices is found to be much lower than that from poled devices (Figure S31, Supporting Information).

The variations in the voltage outputs of these **1**-TPU films can be understood as follows. During the piezoelectric impact stress and release operation, free electrons produced at the electrodes will be driven to flow back and forth to screen the induced piezopotential difference and maintain electrostatic equilibrium between the two electrodes. An alternating output voltage is generated to counter the flow of free electrons in an external circuit. The disproportion in the positive and negative voltage peaks can be ascribed to the variation between the external force applied and the restoring force. When the concentration of **1** is increased, an augmentation in the Maxwell−Wagner−Sillars (MWS) phenomena takes place due to the increase in the interface area.[57] A further increase in the piezoelectric content beyond a threshold limit, however, results in the aggregation of the particles. Although this effect improves permittivity, it also causes the field concentration effect and dipole mobility in an adverse way, leading to a decrease in the output performance.[56,58,59] The scanning electron microscopy (SEM) images recorded on all the **1**-TPU composites show a homogeneous distribution of **1** in the TPU matrix at lower concentrations and indicate the aggregate formation for particle loadings of 10 wt % and above (Figure S32, Supporting Information). To corroborate this, the dielectric permittivity values of all the composite films of **1**-TPU were measured and compared. These measurements showed an increase in the ε' values for up to 5 wt % of **1** in the polymer matrix. However, it was found to decrease in the higher 10 and 15 wt % composites, confirming a reduction of the bulk polarization in them (Figures S33−S35 Supporting Information).

To further confirm the concentration effect of **1** on the device output characteristics, direct piezoelectric coefficient (d_{33}) measurements were performed using the Berlincourt method. The d_{33} values were extracted by a quasi-static piezometer on the various wt % composite films of **1** with an externally applied force of 0.25 N, which operates at a frequency of 110 Hz. These measurements yielded the d_{33} values of 4.20, 11.70, 9.06, and 3.30 pC/N for the composite films 1, 5, 10, and 15 wt % **1**-TPU, respectively (Figure 6c and Figure S36, Supporting Information). Notably, the highest d_{33} value of 11.70 pC/N is acquired for the best performing 5 wt % **1**-TPU film. Also, the observed trends in the d_{33} values again validate the reduction of dipoles due to the increase in the concentration of the particles beyond the optimal loading, which correlates well with the V_{oc} values obtained for the **1**-TPU composite devices.

To determine the appropriate impedance matching for the working efficiency, the electrical output responses (such as voltage, current density, and power density) for the best performing device (5 wt %) were extracted by employing various resistors ranging from 0.1 to 50 MΩ (Figure 6d). The applied pushing force and frequency were maintained constant during the measurements at 40 N and 17 Hz, respectively. With an increment in the load resistance, the output voltages (V) of the 5 wt % **1**-TPU device were found to increase. Concomitantly, the peak-to-peak current density (J) values of the **1**-TPU device are decreased from 15.5 to 0.8 $\mu A/cm^2$, with an increase in the resistance loads from 0.1 to 50 MΩ due to the ohmic loss (Figure S37, Supporting Information). Furthermore, the instantaneous peak power density ($P = V \times J$) of the device was calculated, as shown in Figure 6d. The highest power density value of 14.6 $\mu W/cm^2$ was obtained at 1 MΩ for the 5 wt % **1**-TPU, which is identified as an optimized matching resistance useful for real-life applications. The fatigue experiments on this 5 wt % composite device showed substantial durability exhibiting the retention of the open-circuit voltages even after 400 cycles with a constant external impact of 40 N (Figure S38, Supporting Information).

Despite the fact that metal−organic frameworks (MOFs) and coordination polymers have been utilized in the past as mechanical energy harvesters, most of them have been employed either as additives to PVDF, to enhance its performance via the enhancement of its electroactive β-phase, or as triboelectric nanogenerators.[60,61] However, there are only a few examples of piezoelectric nanogenerators known that employ MOFs or coordination polymers. Recently, Gazit and co-workers have demonstrated nanogenerators constructed from a Zn-peptide-based coordination polymer, in which the output performance was governed by the choice of guest molecules.[62] In this regard, the 5 wt % **1**-TPU device

https://doi.org/10.1021/acssuschemeng.2c02296
ACS Sustainable Chem. Eng. 2022, 10, 9911−9920

exhibits much higher output voltage and power density values, promising the utility of such neutral coordination polymers for future technological applications (Table S4, Supporting Information).

The energy storage efficacy of the **1**-TPU 5 wt % device was further examined through the charging of capacitors with different capacitance values. A full-wave bridge rectifier circuit was employed to connect the device to the capacitor, which converts the ac potentials to dc voltages (Figure 7a). The

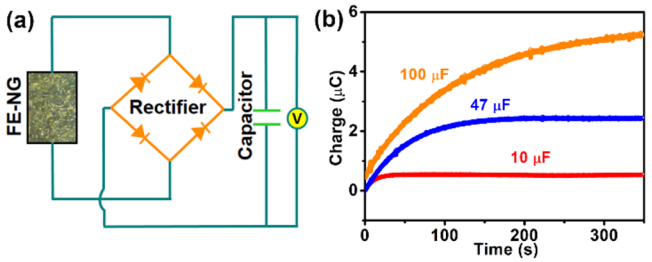

Figure 7. (a) Drawing representing the charging of a capacitor using a **1**-TPU device connected through a full-wave bridge rectifier circuit. (b) Calculated charge of the 5 wt % **1**-TPU device at different load capacitances.

voltages in the capacitors were found to increase as a function of time, and the obtained saturation voltages were found to be very close for most of the load capacitors (Figure S39, Supporting Information). The charging rate is higher for a lower value capacitor as its saturation charge is attained quicker than the other higher loading capacitors. Note that the voltage measured across these capacitors is much lower than the corresponding output voltage due to the voltage consumed in rectification of the diodes and/or leakage of the stored energy in the capacitors.[63,64] Furthermore, the stored charges (Q) on the capacitors (C_L) were calculated by the formula $Q = C_L V$ (Figure 7b). A linear relationship between the strength of the load capacitor and the storage capacity is observed in all of them, showing a gradual increase in the energy storage until the curves become saturated.[65,66] Again, the 10 μF capacitor stores only a small amount of charge and attains the saturation value very quickly. A maximum stored charge of 5.22 μC is noted for the highest rated 100 μF capacitor at a given time of 350 s.

CONCLUSIONS

In summary, we have synthesized a neutral noncentrosymmetric one-dimensional coordination network **1** that exhibits both piezo- and ferroelectric properties. An electromechanical coefficient value of 19.4 pm/V extracted from the PFM measurements is remarkable for its neutral framework structure. The existence of a dipole moment in **1** can be tracked down to the distortions of the Zn(II) center, as inferred from preliminary DFT calculations. Also, the P-E loop measurements yielded a P_r value of 8.04 μC/cm^2, supporting its ferroelectric properties. Furthermore, flexible composite materials of **1** were prepared and employed as piezoelectric energy devices. The highest open-circuit voltage of 5.6 V and power density output of 14.6 μW/cm^2 were recorded for the optimized champion device containing 5 wt % of **1** in the TPU matrix. The potential of this framework-based device for small-scale energy storage was demonstrated via capacitor charging experiments. These findings demonstrate the potential of lead-free ferroelectric metal−organic frameworks with lightweight metal ions for fabricating piezoelectric nanogenerator devices for use in future multifunctional electronics.

ASSOCIATED CONTENT

Supporting Information

The Supporting Information is available free of charge at https://pubs.acs.org/doi/10.1021/acssuschemeng.2c02296.

Data pertaining to experimental details, schemes, structural illustrations, tables, VT-PXRD and VT-SCXRD, TGA/DTA, ferro- and piezoelectric, dielectric measurements and fabrication of the device, characterization, and analyses (PDF)

X-ray crystallographic data for **1** (CIF)

X-ray crystallographic data for **L** (CIF)

X-ray crystallographic data for $\mathbf{L^1H_2}$ (CIF)

AUTHOR INFORMATION

Corresponding Authors

Balu Praveenkumar − *PZT Centre, Armament Research and Development Establishment, Pune 411021, India*; Email: praveenkumar@arde.drdo.in

Jan K. Zaręba − *Institute of Advanced Materials, Wroclaw University of Science and Technology, 50-370 Wroclaw, Poland*; orcid.org/0000-0001-6117-6876; Email: jan.zareba@pwr.edu.pl

Dinesh Kabra − *Department of Physics, Indian Institute of Technology, Mumbai 400076, India*; orcid.org/0000-0001-5256-1465; Email: dkabra@phy.iitb.ac.in

Satishchandra Ogale − *Centre for Energy Science and Department of Physics, Indian Institute of Science Education and Research (IISER), Pune 411008, India; Research Institute for Sustainable Energy (RISE), TCG Centres for Research and Education in Science and Technology (TCG-CREST), Kolkata 700091, India*; orcid.org/0000-0001-5593-9339; Email: satishogale@iiserpune.ac.in

Ramamoorthy Boomishankar − *Department of Chemistry, Indian Institute of Science Education and Research (IISER), Pune 411008, India; Centre for Energy Science, Indian Institute of Science Education and Research (IISER), Pune 411008, India*; orcid.org/0000-0002-5933-4414; Email: boomi@iiserpune.ac.in

Authors

Neetu Prajesh − *Department of Chemistry, Indian Institute of Science Education and Research (IISER), Pune 411008, India; Centre for Energy Science, Indian Institute of Science Education and Research (IISER), Pune 411008, India*

Vijay Bhan Sharma − *Department of Physics, Indian Institute of Technology, Mumbai 400076, India*

Shatruhan Singh Rajput − *Department of Physics, Indian Institute of Science Education and Research (IISER), Pune 411008, India*

Chandan Kumar Singh − *Department of Physics, Indian Institute of Science Education and Research (IISER), Pune 411008, India*

Prashant Dixit − *PZT Centre, Armament Research and Development Establishment, Pune 411021, India*

Complete contact information is available at: https://pubs.acs.org/10.1021/acssuschemeng.2c02296

Notes

The authors declare no competing financial interest.

■ ACKNOWLEDGMENTS

This work was funded by SERB, India, by grant no. CRG/2019/004615 (R.B.) and the Nanomission Project, DST, India, via grant no. SR/NM/TP-13/2016 (S.O. and R.B.). R.B. thanks the SERB-STAR Award via grant no. STR/2021/000016. N.P. thanks the CSIR, India, for the fellowship. S.O. and D.K. acknowledge the funding from the UK-India SUNRISE program. J.K.Z. thanks the Academia Iuvenum, Wroclaw University of Science and Technology for support. The IISER-Pune PARAM Brahma Facility under the Government of India aided National Supercomputing Mission is gratefully acknowledged.

■ REFERENCES

(1) Kagan, C. R.; Mitzi, D. B.; Dimitrakopoulos, C. D. Organic-Inorganic Hybrid Materials as Semiconducting Channels in Thin-Film Field-Effect Transistors. *Science* **1999**, *286*, 945−947.

(2) Lee, M. M.; Teuscher, J.; Miyasaka, T.; Murakami, T. N.; Snaith, H. J. Efficient Hybrid Solar Cells Based on Meso-Superstructured Organometal Halide Perovskites. *Science* **2012**, *338*, 643−647.

(3) Han, S.-T.; Zhou, Y.; Roy, V. A. L. Towards the Development of Flexible Non-Volatile Memories. *Adv. Mater.* **2013**, *25*, 5425−5449.

(4) Scott, J. F.; Paz de Araujo, C. A. Ferroelectric Memories. *Science* **1989**, *246*, 1400−1405.

(5) Vanderah, T. A. Talking Ceramics. *Science* **2002**, *298*, 1182−1184.

(6) Tayi, A. S.; Kaeser, A.; Matsumoto, M.; Aida, T.; Stupp, S. I. Supramolecular ferroelectrics. *Nat. Chem.* **2015**, *7*, 281−294.

(7) Zhang, W.; Xiong, R.-G. Ferroelectric Metal−Organic Frameworks. *Chem. Rev.* **2012**, *112*, 1163−1195.

(8) Liu, H.-Y.; Zhang, H.-Y.; Chen, X.-G.; Xiong, R.-G. Molecular Design Principles for Ferroelectrics: Ferroelectrochemistry. *J. Am. Chem. Soc.* **2020**, *142*, 15205−15218.

(9) Vijayakanth, T.; Liptrot, D. J.; Gazit, E.; Boomishankar, R.; Bowen, C. R. Recent Advances in Organic and Organic−Inorganic Hybrid Materials for Piezoelectric Mechanical Energy Harvesting. *Adv. Funct. Mater.* **2022**, *32*, 2109492.

(10) Lu, L.; Ding, W.; Liu, J.; Yang, B. Flexible PVDF based piezoelectric nanogenerators. *Nano Energy* **2020**, *78*, 105251.

(11) Zhang, Y.; Hopkins, M. A.; Liptrot, D. J.; Khanbareh, H.; Groen, P.; Zhou, X.; Zhang, D.; Bao, Y.; Zhou, K.; Bowen, C. R.; Carbery, D. R. Harnessing Plasticity in an Amine-Borane as a Piezoelectric and Pyroelectric Flexible Film. *Angew. Chem., Int. Ed.* **2020**, *59*, 7808−7812.

(12) Bowen, C. R.; Kim, H. A.; Weaver, P. M.; Dunn, S. Piezoelectric and ferroelectric materials and structures for energy harvesting applications. *Energy Environ. Sci.* **2014**, *7*, 25−44.

(13) Pandey, R.; Sb, G.; Grover, S.; Singh, S. K.; Kadam, A.; Ogale, S.; Waghmare, U. V.; Rao, V. R.; Kabra, D. Microscopic Origin of Piezoelectricity in Lead-Free Halide Perovskite: Application in Nanogenerator Design. *ACS Energy Lett.* **2019**, *4*, 1004−1011.

(14) Xu, L.; Mu, X.; Chen, X.-G.; Zhang, H.-Y.; Xiong, R.-G. Organic Enantiomeric Ferroelectrics with High Piezoelectric Performance: Imidazolium L- and D-Camphorsulfonate. *Chem. Mater.* **2021**, *33*, 5769−5779.

(15) Vivekananthan, V.; Alluri, N. R.; Purusothaman, Y.; Chandrasekhar, A.; Kim, S.-J. A flexible, planar energy harvesting device for scavenging road side waste mechanical energy via the synergistic piezoelectric response of $K_{0.5}Na_{0.5}NbO_3$-$BaTiO_3$/PVDF composite films. *Nanoscale* **2017**, *9*, 15122−15130.

(16) Vats, G.; Kumar, A.; Ortega, N.; Bowen, C. R.; Katiyar, R. S. Giant pyroelectric energy harvesting and a negative electrocaloric effect in multilayered nanostructures. *Energy Environ. Sci.* **2016**, *9*, 1335−1345.

(17) Das, S.; Xu, S.; Ben, T.; Qiu, S. Chiral Recognition and Separation by Chirality-Enriched Metal−Organic Frameworks. *Angew. Chem., Int. Ed.* **2018**, *57*, 8629−8633.

(18) Alaerts, L.; Kirschhock, C. E. A.; Maes, M.; van der Veen, M. A.; Finsy, V.; Depla, A.; Martens, J. A.; Baron, G. V.; Jacobs, P. A.; Denayer, J. F. M.; De Vos, D. E. Selective Adsorption and Separation of Xylene Isomers and Ethylbenzene with the Microporous Vanadium(IV) Terephthalate MIL-47. *Angew. Chem., Int. Ed.* **2007**, *46*, 4293−4297.

(19) Morris, W.; Briley, W. E.; Auyeung, E.; Cabezas, M. D.; Mirkin, C. A. Nucleic Acid−Metal Organic Framework (MOF) Nanoparticle Conjugates. *J. Am. Chem. Soc.* **2014**, *136*, 7261−7264.

(20) Xiao, J.; Liu, J.; Liu, M.; Ji, G.; Liu, Z. Fabrication of a Luminescence-Silent System Based on a Post-Synthetic Modification Cd-MOFs: A Highly Selective and Sensitive Turn-on Luminescent Probe for Ascorbic Acid Detection. *Inorg. Chem.* **2019**, *58*, 6167−6174.

(21) Zaręba, J. K.; Nyk, M.; Samoć, M. Nonlinear Optical Properties of Emerging Nano- and Microcrystalline Materials. *Adv. Opt. Mater.* **2021**, *9*, 2100216.

(22) Medishetty, R.; Zaręba, J. K.; Mayer, D.; Samoć, M.; Fischer, R. A. Nonlinear optical properties, upconversion and lasing in metal−organic frameworks. *Chem. Soc. Rev.* **2017**, *46*, 4976−5004.

(23) Mingabudinova, L. R.; Vinogradov, V. V.; Milichko, V. A.; Hey-Hawkins, E.; Vinogradov, A. V. Metal−organic frameworks as competitive materials for non-linear optics. *Chem. Soc. Rev.* **2016**, *45*, 5408−5431.

(24) Horiuchi, S.; Tokunaga, Y.; Giovannetti, G.; Picozzi, S.; Itoh, H.; Shimano, R.; Kumai, R.; Tokura, Y. Above-room-temperature ferroelectricity in a single-component molecular crystal. *Nature* **2010**, *463*, 789−792.

(25) Dong, X.-Y.; Li, B.; Ma, B.-B.; Li, S.-J.; Dong, M.-M.; Zhu, Y.-Y.; Zang, S.-Q.; Song, Y.; Hou, H.-W.; Mak, T. C. W. Ferroelectric Switchable Behavior through Fast Reversible De/adsorption of Water Spirals in a Chiral 3D Metal−Organic Framework. *J. Am. Chem. Soc.* **2013**, *135*, 10214−10217.

(26) Hang, T.; Zhang, W.; Ye, H.-Y.; Xiong, R.-G. Metal−organic complex ferroelectrics. *Chem. Soc. Rev.* **2011**, *40*, 3577−3598.

(27) Zhang, W.; Ye, H.-Y.; Xiong, R.-G. Metal-organic coordination compounds for potential ferroelectrics. *Coord. Chem. Rev.* **2009**, *253*, 2980−2997.

(28) Srivastava, A. K.; Divya, P.; Praveenkumar, B.; Boomishankar, R. Potentially Ferroelectric {$CuIIIL_2$}n Based Two-Dimensional Framework Exhibiting High Polarization and Guest-Assisted Dielectric Anomaly. *Chem. Mater.* **2015**, *27*, 5222−5229.

(29) Srivastava, A. K.; Praveenkumar, B.; Mahawar, I. K.; Divya, P.; Shalini, S.; Boomishankar, R. Anion Driven [$CuIIL_2$]n Frameworks: Crystal Structures, Guest-Encapsulation, Dielectric, and Possible Ferroelectric Properties. *Chem. Mater.* **2014**, *26*, 3811−3817.

(30) Srivastava, A. K.; Vijayakanth, T.; Divya, P.; Praveenkumar, B.; Steiner, A.; Boomishankar, R. Altering polarization attributes in ferroelectric metallo-cavitands by varying hydrated alkali-metal guest cations. *J. Mater. Chem. C* **2017**, *5*, 7352−7359.

(31) Yadav, A.; Srivastava, A. K.; Kulkarni, P.; Divya, P.; Steiner, A.; Praveenkumar, B.; Boomishankar, R. Anion-induced ferroelectric polarization in a luminescent metal−organic cage compound. *J. Mater. Chem. C* **2017**, *5*, 10624−10629.

(32) Yadav, A.; Kulkarni, P.; Praveenkumar, B.; Steiner, A.; Boomishankar, R. Hierarchical Frameworks of Metal−Organic Cages with Axial Ferroelectric Anisotropy. *Chem. − Eur. J.* **2018**, *24*, 14639−14643.

(33) Prajesh, N.; Yadav, A.; Gourkhede, R.; Praveenkumar, B.; Steiner, A.; Boomishankar, R. Ferroelectric Behavior of an Octahedral Metal-Ligand Cage and Its 2D-Connected Cage Framework. *Chem. − Asian J.* **2020**, *15*, 3275−3280.

(34) Xue, F.; Cao, J.; Li, X.; Feng, J.; Tao, M.; Xue, B. Continuous-flow synthesis of MIL-53(Cr) with a polar linker: probing the nanoscale piezoelectric effect. *J. Mater. Chem. C* **2021**, *9*, 7568−7574.

https://doi.org/10.1021/acssuschemeng.2c02296
ACS Sustainable Chem. Eng. 2022, 10, 9911−9920

(35) Sun, Y.; Hu, Z.; Zhao, D.; Zeng, K. Probing nanoscale functionalities of metal−organic framework nanocrystals. *Nanoscale* **2017**, *9*, 12163−12169.
(36) Sun, Y.; Gao, J.; Cheng, Y.; Zhang, Y.-W.; Zeng, K. Design of the Hybrid Metal−Organic Frameworks as Potential Supramolecular Piezo-/Ferroelectrics. *J. Phys. Chem. C* **2019**, *123*, 3122−3129.
(37) Giannozzi, P.; Baroni, S.; Bonini, N.; Calandra, M.; Car, R.; Cavazzoni, C.; Ceresoli, D.; Chiarotti, G. L.; Cococcioni, M.; Dabo, I.; Dal Corso, A.; de Gironcoli, S.; Fabris, S.; Fratesi, G.; Gebauer, R.; Gerstmann, U.; Gougoussis, C.; Kokalj, A.; Lazzeri, M.; Martin-Samos, L.; Marzari, N.; Mauri, F.; Mazzarello, R.; Paolini, S.; Pasquarello, A.; Paulatto, L.; Sbraccia, C.; Scandolo, S.; Sclauzero, G.; Seitsonen, A. P.; Smogunov, A.; Umari, P.; Wentzcovitch, R. M. QUANTUM ESPRESSO: a modular and open-source software project for quantum simulations of materials. *J. Phys.: Condens. Matter* **2009**, *21*, 395502.
(38) Hamann, D. R. Optimized norm-conserving Vanderbilt pseudopotentials. *Phys. Rev. B* **2013**, *88*, No. 085117.
(39) Perdew, J. P.; Burke, K.; Ernzerhof, M. Generalized Gradient Approximation Made Simple. *Phys. Rev. Lett.* **1996**, *77*, 3865−3868.
(40) Momma, K.; Izumi, F. VESTA 3 for three-dimensional visualization of crystal, volumetric and morphology data. *J. Appl. Crystallogr.* **2011**, *44*, 1272−1276.
(41) Addison, A. W.; Rao, T. N.; Reedijk, J.; van Rijn, J.; Verschoor, G. C. Synthesis, structure, and spectroscopic properties of copper(II) compounds containing nitrogen−sulphur donor ligands; the crystal and molecular structure of aqua[1,7-bis(N-methylbenzimidazol-2′-yl)-2,6-dithiaheptane]copper(II) perchlorate. *J. Chem. Soc., Dalton Trans.* **1984**, 1349−1356.
(42) King-Smith, R. D.; Vanderbilt, D. Theory of polarization of crystalline solids. *Phys. Rev. B* **1993**, *47*, 1651−1654.
(43) Neaton, J. B.; Ederer, C.; Waghmare, U. V.; Spaldin, N. A.; Rabe, K. M. First-principles study of spontaneous polarization in multiferroic $BiFeO_3$. *Phys. Rev. B* **2005**, *71*, No. 014113.
(44) Spaldin, N. A. A beginner's guide to the modern theory of polarization. *J. Solid State Chem.* **2012**, *195*, 2−10.
(45) Di Sante, D.; Stroppa, A.; Jain, P.; Picozzi, S. Tuning the Ferroelectric Polarization in a Multiferroic Metal−Organic Framework. *J. Am. Chem. Soc.* **2013**, *135*, 18126−18130.
(46) Kurtz, S. K.; Perry, T. T. A Powder Technique for the Evaluation of Nonlinear Optical Materials. *J. Appl. Phys.* **1968**, *39*, 3798−3813.
(47) Graja, A. Production of the Second Harmonic of Light in Ammonium Pentaborate and other Powdered Piezoelectric Crystals. *Phys. Stat. Sol.* **1968**, *27*, K93−K97.
(48) Scott, J. F. Ferroelectrics go bananas. *J. Phys.: Condens. Matter* **2007**, *20*, No. 021001.
(49) Liao, W.-Q.; Zhao, D.; Tang, Y.-Y.; Zhang, Y.; Li, P.-F.; Shi, P.-P.; Chen, X.-G.; You, Y.-M.; Xiong, R.-G. A molecular perovskite solid solution with piezoelectricity stronger than lead zirconate titanate. *Science* **2019**, *363*, 1206−1210.
(50) You, Y.-M.; Liao, W.-Q.; Zhao, D.; Ye, H.-Y.; Zhang, Y.; Zhou, Q.; Niu, X.; Wang, J.; Li, P.-F.; Fu, D.-W.; Wang, Z.; Gao, S.; Yang, K.; Liu, J.-M.; Li, J.; Yan, Y.; Xiong, R.-G. An organic-inorganic perovskite ferroelectric with large piezoelectric response. *Science* **2017**, *357*, 306−309.
(51) Vijayakanth, T.; Ram, F.; Praveenkumar, B.; Shanmuganathan, K.; Boomishankar, R. Piezoelectric Energy Harvesting from a Ferroelectric Hybrid Salt $[Ph_3MeP]_4[Ni(NCS)_6]$ Embedded in a Polymer Matrix. *Angew. Chem., Int. Ed.* **2020**, *59*, 10368−10373.
(52) Jeong, C. K.; Park, K.-I.; Ryu, J.; Hwang, G.-T.; Lee, K. J. Large-Area and Flexible Lead-Free Nanocomposite Generator Using Alkaline Niobate Particles and Metal Nanorod Filler. *Adv. Funct. Mater.* **2014**, *24*, 2620−2629.
(53) Siddiqui, S.; Kim, D.-I.; Duy, L. T.; Nguyen, M. T.; Muhammad, S.; Yoon, W.-S.; Lee, N.-E. High-performance flexible lead-free nanocomposite piezoelectric nanogenerator for biomechanical energy harvesting and storage. *Nano Energy* **2015**, *15*, 177−185.
(54) Singh, S. K.; Muduli, S.; Dhakras, D.; Pandey, R.; Babar, R.; Singh, A.; Kabra, D.; Kabir, M.; Boomishankar, R.; Ogale, S. High power mechanical energy harvester based on exfoliated black phosphorous−polymer composite and its multiple applications. *Sustain. Energy Fuels* **2019**, *3*, 1943−1950.
(55) Wu, M.; Zheng, T.; Zheng, H.; Li, J.; Wang, W.; Zhu, M.; Li, F.; Yue, G.; Gu, Y.; Wu, J. High-performance piezoelectric-energy-harvester and self-powered mechanosensing using lead-free potassium−sodium niobate flexible piezoelectric composites. *J. Mater. Chem. A* **2018**, *6*, 16439−16449.
(56) Park, K.-I.; Lee, M.; Liu, Y.; Moon, S.; Hwang, G.-T.; Zhu, G.; Kim, J. E.; Kim, S. O.; Kim, D. K.; Wang, Z. L.; Lee, K. J. Flexible Nanocomposite Generator Made of BaTiO3 Nanoparticles and Graphitic Carbons. *Adv. Mater.* **2012**, *24*, 2999−3004.
(57) Kim, S.; Gupta, M. K.; Lee, K. Y.; Sohn, A.; Kim, T. Y.; Shin, K.-S.; Kim, D.; Kim, S. K.; Lee, K. H.; Shin, H.-J.; Kim, D.-W.; Kim, S.-W. Transparent Flexible Graphene Triboelectric Nanogenerators. *Adv. Mater.* **2014**, *26*, 3918−3925.
(58) Lee, K. Y.; Kim, D.; Lee, J.-H.; Kim, T. Y.; Gupta, M. K.; Kim, S.-W. Unidirectional High-Power Generation via Stress-Induced Dipole Alignment from $ZnSnO_3$ Nanocubes/Polymer Hybrid Piezoelectric Nanogenerator. *Adv. Funct. Mater.* **2014**, *24*, 37−43.
(59) Nie, J.; Zhu, L.; Zhai, W.; Berbille, A.; Li, L.; Wang, Z. L. Flexible Piezoelectric Nanogenerators Based on P(VDF-TrFE)/$CsPbBr_3$ Quantum Dot Composite Films. *ACS Appl. Electron. Mater.* **2021**, *3*, 2136−2144.
(60) Khandelwal, G.; Chandrasekhar, A.; Maria Joseph Raj, N. P.; Kim, S.-J. Metal−Organic Framework: A Novel Material for Triboelectric Nanogenerator−Based Self-Powered Sensors and Systems. *Adv. Energy Mater.* **2019**, *9*, 1803581.
(61) Hajra, S.; Sahu, M.; Padhan, A. M.; Lee, I. S.; Yi, D. K.; Alagarsamy, P.; Nanda, S. S.; Kim, H. J. A Green Metal−Organic Framework-Cyclodextrin MOF: A Novel Multifunctional Material Based Triboelectric Nanogenerator for Highly Efficient Mechanical Energy Harvesting. *Adv. Funct. Mater.* **2021**, *31*, 2101829.
(62) Chen, Y.; Guerin, S.; Yuan, H.; O'Donnell, J.; Xue, B.; Cazade, P.-A.; Haq, E. U.; Shimon, L. J. W.; Rencus-Lazar, S.; Tofail, S. A. M.; Cao, Y.; Thompson, D.; Yang, R.; Gazit, E. Guest Molecule-Mediated Energy Harvesting in a Conformationally Sensitive Peptide−Metal Organic Framework. *J. Am. Chem. Soc.* **2022**, *144*, 3468−3476.
(63) Yan, J.; Jeong, Y. G. High Performance Flexible Piezoelectric Nanogenerators based on $BaTiO_3$ Nanofibers in Different Alignment Modes. *ACS Appl. Mater. Interfaces* **2016**, *8*, 15700−15709.
(64) Xu, S.; Hansen, B. J.; Wang, Z. L. Piezoelectric-nanowire-enabled power source for driving wireless microelectronics. *Nat. Commun.* **2010**, *1*, 93.
(65) Niu, S.; Wang, Z. L. Theoretical systems of triboelectric nanogenerators. *Nano Energy* **2015**, *14*, 161−192.
(66) Niu, S.; Liu, Y.; Zhou, Y. S.; Wang, S.; Lin, L.; Wang, Z. L. Optimization of Triboelectric Nanogenerator Charging Systems for Efficient Energy Harvesting and Storage. *IEEE Trans. Electron Devices* **2015**, *62*, 641−647.

https://doi.org/10.1021/acssuschemeng.2c02296
ACS Sustainable Chem. Eng. 2022, 10, 9911−9920